Check for updates

Electromechanically active pair dynamics in a Gd-doped ceria single crystal†

Simone Santucci, [ID] *[a] Haiwu Zhang,[a] Ahsanul Kabir, [ID] [a] Carlo Marini,[b] Simone Sanna, [ID] [a] Jyn Kyu Han,[a] Gregor Ulbrich,[c] Eva Maria Heppke,[c] Ivano E. Castelli[a] and Vincenzo Esposito [ID] *[a]

Oxygen-defective ceria, *e.g.* Gd-doped ceria, shows giant electromechanical properties related to a complex local rearrangement of its lattice. Although they are not entirely identified, the electroactive mechanisms arise from cation and oxygen vacancy (V_O) pairs (*i.e.* Ce–V_O), and the local structural elastic distortion in their surroundings. Here, we study the geometry and behaviour of Ce–V_O pairs in a grain boundary-free bulk $Ce_{0.9}Gd_{0.1}O_{1.95}$ single crystal under an AC electric field of *ca.* 11 kV cm^{-1}. The analysis was carried out through X-ray absorption spectroscopy (XAS) techniques at the Ce L-III edge. Using Density Functional Theory (DFT) calculations, we investigated the effects of the strain on density of states and orbitals at the valence band edge. Our research indicates that electrostriction increases at low temperatures. The electromechanical strain has a structural nature and can rise by one order of magnitude, *i.e.*, from 5×10^{-4} at room temperature to 5×10^{-3} at −193 °C, due to an increase in the population of the electrically active pairs. At a constant V_O concentration, the material can thus configure heterogeneous pairs and elastic nanodomains that are either mechanically responsive or not.

Introduction

Gadolinium-doped ceria (CGO) and other oxygen-defective oxides have recently attracted attention for their outstanding "non-classical" giant electrostriction.[1–5] However, the electromechanical mechanisms in the materials remain unclear. Several studies have used X-ray Absorption Spectroscopy (XAS) to show the dynamics of non-classical electrostriction related to the defect structure of the CGO lattice.[1,6,7] Doped ceria accommodates many randomly distributed double-positive oxygen vacancies (V_O, *i.e.* $V_O^{\bullet\bullet}$, according to the Kröger–Vink notation). Doping the material with 20 mol% Gd^{3+} produces an oxygen vacancy concentration of 10% while maintaining the cubic fluorite symmetry of the lattice.[8–10] At such a high doping level, the vacancy concentration depends only on the extrinsic dopant amount, and so it is considered constant.

Each oxygen vacancy causes a local electro-steric distortion and a deviation in the lattice. At the first level of analysis, the

[a] Department of Energy Conversion and Storage, Technical University of Denmark, Fysikvej, Building 310, 2800 Kgs., Lyngby, Denmark. E-mail: vies@dtu.dk, sisan@dtu.dk

[b] ALBA Synchrotron, Carrer de la llum, 2-26Cerdanyola del Vallès, 08290 Barcelona, Spain

[c] Institut für Chemie, Technische Universität Berlin, Straße des 17, Juni 135, 10623 Berlin, Germany

† Electronic supplementary information (ESI) available. See DOI: 10.1039/d1cp00748c

Ce_{Ce}–V_O pairs impose local elastic and charge fields[1,6] which relax through the crystal. When an electric field is applied, both the Ce_{Ce}–V_O pair and the cluster in its vicinity experience strain, leading to a macroscopic expansion.[6,11] Such an effect is different from "classical" electrostriction mechanisms, proposed by Newnham, where the distortion comprises the whole structure.[11] As a result, CGO and other defective fluorites can display outstanding electrostrictive behaviour.

The definition of Ce_{Ce}–V_O includes both 4+ host cations ($[Ce_{Ce}^x − V_O^{\bullet\bullet}]$) and the polarised 3+ species-vacancies pairs ($[Gd_{Ce}' − V_O^{\bullet\bullet}]$ and the $[Ce_{Ce}' − V_O^{\bullet\bullet}]$). However, assuming that the oxygen defects are random in the lattice and their mobility is nearly null at low temperature, Ce_{Ce}–V_O pairs embody the average of all the configurations in the crystal.

For epitaxial thin CGO films with controlled orientation, the electrostriction coefficient, *e.g.* M_{33}, is between 10^{-17} and 10^{-16} m^2 V^{-2}.[11] This value surpasses the best piezoelectric electrostrictor, $Pb(Mn_{1/3}Nb_{2/3})O_3$ (PMN), which has typical M_{33} values of 10^{-18} m^2 V^{-2}.[12] In epitaxial films, electrostriction is enhanced by aligning the applied electric field to the Ce_{Ce}–V_O pairs.[11] In polycrystalline thin films[1–3,5,13] and bulk ceramics,[4,14] the presence of grain boundaries and disorder leads to randomly oriented Ce_{Ce}–V_O pairs. Further, crystalline disorder introduces a wide range of electrosteric factors with a complex variety of configurations and electromechanical responses.[14]

The vacancy's elastic response to an electric field is indeed related to the temperature.[10,15–17] In thin-films, electrostrictive

This journal is © the Owner Societies 2021

Phys. Chem. Chem. Phys., 2021, **23**, 11233–11239 | **11233**

performances do not change from 25° to 75 °C.[18,19] However, at high temperatures, defects diffuse in the lattice,[20,21] hindering electrostriction and leading to ionic conduction.[1,18,19] Simultaneously with vacancy mobility, there is an increase of secondary "non-structural" effects such as asymmetric electrode polarisation, chemical reactions and charge injection at the film/electrode interface.[18] These side-processes hinder a clear definition of the driving mechanisms in electrostriction, reducing performance and often leading to the mechanical failure of these materials.[1,3,19]

Electrostriction measurements at low temperatures are still not available in the literature. However, the suppression of thermally driven mechanisms can help the analysis of this phenomenon. Some studies have already unveiled some other typical oxygen vacancies and Ce_{Ce}–V_O pair effects at low temperatures.[6,14,22,23] In CGO thin films, cooling to −123 °C leads to a reduction of the dielectric constant as charge-hopping decreases (exponentially).[22] For temperatures below −200 °C,[22] the dielectric constant of CGO is both temperature- and frequency-independent, with a value of $\varepsilon_r = 20 \pm 2$. Such an effect likely arises from low temperature triggered fluctuations in the ordering of the Ce_{Ce}–V_O pairs.[22] Such a feature is particularly relevant for electrostriction; if the total concentration of the vacancies is kept constant, pairs and their domains can change their configuration in the presence of intense electric fields. Local lattice distortions also occur in bulk ceria doped with other trivalent cations (Y or Sc). At low temperatures of about −160 °C, such a structural distortion arises from an asymmetry in the cation/anion pair potential.[23] This kind of distortion likely comprises a broader cluster of atoms, leading to nanodomain-like effects. Moreover, the cage of eight O^{2-} ions surrounding the dopant cation assumes an asymmetrical configuration.[23] As electrostriction in CGO results from lattice distortions around the oxygen vacancy,[6,14] low-temperature dynamics are likely to influence the mechanisms which produce this effect.

In the present paper, we investigate the structural and chemical environments in the vicinity of vacancies by X-ray Absorption Spectroscopy (XAS). We report the electrostriction property of 10 mol% Gd-doped CeO_2 in a single crystal, *i.e.* free of pair-disorder electrosteric interactions at a constant concentration (extrinsic conditions). We use X-ray absorption techniques to characterize the local distortion dynamics behaviour of Ce–O chains under an electric field over a wide temperature range (from RT down to −194 °C). We apply *in situ* an electric field to clarify the CeO_2 crystalline cell's effect towards the geometrical deformation caused by Ce–O bond length non-constant distribution around the defects.[6,7] Such results give new insights into the mechanism of the outstanding non-classic electrostriction properties in this family of materials.

Experimental

Single crystal synthesis

A 10 mol% CGO single crystal (CGO20) was grown using the skull melting technique. Details are reported for zirconia and ceria in other papers.[24–27] The sample selected for the test was $4 \times 4 \times 0.7$ mm thick, with gold electrodes sputtered on two opposite faces normal to the [111] direction.

Structural, electrical and electrostriction characterization

We performed *ex situ* electrostriction measurements at room temperature *via* laser interferometry microscopy (Nano Vibration Analyzer – SIOS Meßtechnik GmbH) (Fig. S1, ESI†). Details of the experimental setup and configurations are in the ESI.† [3,11] Sample investigation included X-ray diffraction (Fig. S2, ESI†) and electrochemical impedance spectroscopy (Fig. S3, ESI†). Experimental details on impedance spectroscopy method are in a previous publication.[14]

X-Ray absorption spectroscopy

For the XAS analysis, we performed the experiments at the Claess beamline in Elettra synchrotron. The experimental details can be found in the literature.[28] The experiments were performed at the Ce L-III-edge (≈ 5.7 keV) on a CGO single crystal in fluorescence mode, using a Si(111) double crystal monochromator with a flux of 10^{12} photons per sec. We acquired data with a multi-channel SDD that allows up to six spectra for each measurement. 15–20 acquisitions were used for the analysis, each performed with all six available channels merged to increase the signal/noise ratio. The energy resolution was 0.3 eV. The spectra were normalized using the Athena and Artemis software, within the IFEFFIT package.[29] For the temperature control, we conditioned the sample in a cryostat,[28,30,31] cooling with a liquid nitrogen line (LN_2-cryo) passed through the sample holder. The pressure was set to $P \approx 10^{-3}$ mbar to maintain the X-ray beam intensity.

Fig. 1 shows the schematics of the experimental setup. The measurements started at RT and then the sample was cooled to −193 °C, and progressively at −125 °C, −50 °C and 23 °C (RT) at 2 °C min⁻¹. At each temperature, the sample was first equilibrated for 30 min, followed by the XAS measurement without an electric field ("OFF" state) and then with an electric field applied (11 kV cm⁻¹ in the "ON" state). We recorded 24–30 XAS spectra in each state, which were then normalized and merged using Athena software.[29] The final data sets
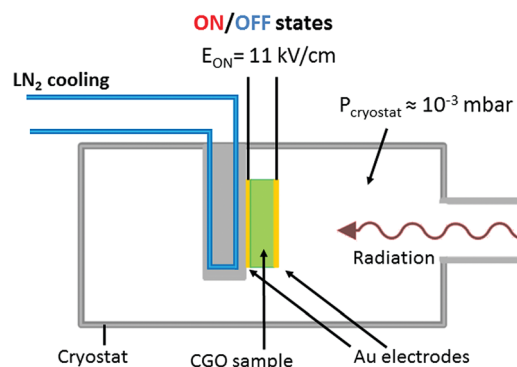

Fig. 1 Schematics of the cryogenic chamber adapted to the *in situ* measurements.

11234 | *Phys. Chem. Chem. Phys.,* 2021, **23**, 11233–11239

This journal is © the Owner Societies 2021

include two spectra (ON and OFF) for each temperature. We used a solid-state detector (Amptek silicon drift (XR-100SDD)) placed at 90 degrees to the incoming beam.[28] The monochromator is a liquid nitrogen-cooled double-crystal FMB-Oxford, Si 111-crystal. The source was a 1 m long wiggler with 25 NdFeB poles. The maximum field was 1.74 T, and the minimum gap was 12.9 mm. The theoretical maximum energy was 70 keV. We applied the electric field with an AIM-TTI TGP 3100 function generator coupled with a Trek 2220 amplifier, which supplied a maximum voltage of 2 kV. To contact the samples inside the chamber, we used cables passed through a vacuum valve with BHV contact on the outside and solder contact inside the cryostat.

Quantitative analysis of X-ray absorption near edge spectroscopy (XANES) spectra was performed to evaluate the difference in the ON and OFF states. This analysis was done by peak Gaussian arc-tg fitting and area calculation. Extended X-ray absorption fine structure (EXAFS) spectroscopy was performed in both ON and OFF states and then the differential spectra $(\Delta\chi(k) = \chi(k)_{on} - \chi(k)_{off})$ were analyzed as described in the Results and the ESI.†

Atomistic simulations

We used Density Functional Theory (DFT) mainly to investigate the effects of strain on the electronic density at the atomistic level. Each simulation was performed using the Perdew–Burke–Ernzerhof (PBE) exchange–correlation functional,[32] as implemented in the GPAW code,[33,34] in the plane wave mode (cutoff energy of 800 eV). We applied a Hubbard+U correction of 4.5 eV to the d-orbitals of Ce. To correctly reproduce the same oxygen vacancy observed in the experiments, we created a supercell by repeating the unit cell of CeO_2 $(2 \times 1 \times 1)$ and modifying the lattice vectors $((2\sqrt{2}, 2\sqrt{2}, 1),(2\sqrt{2}, -2\sqrt{2}, 1),(1, 1, 1))$. We used a Monkhorst pack k-point mesh of $(6 \times 6 \times 6)$ throughout the calculations. We applied the strain in the $[1-1-0]$ direction, and the cell relaxed in the direction perpendicular to the strain. All atomic positions are fully relaxed until the forces are below 0.01 eV Å^{-1}. We used the Atomistic Simulation Environment (ASE) package to work with the structures.[35] We assumed the oxygen vacancies are random, and our calculations did not include Gd explicitly.

Results and discussion

A portion of the single-crystal was cut analyzed by EDS, resulting in chemical purity. Other portions were pulverized, and the XRD analysis indicated a cubic pure fluorite crystal structure with a lattice parameter of 5.4179 Å. This value is slightly larger than what is observed in CGO polycrystalline ceramics, probably due to the absence of grain boundaries in the single-crystals.[25,36] The ESI† includes XRD measurements of the powdered single-crystal and graphical representation of the Rietveld refinement (Fig. S2, ESI†).

The ionic transport at high temperatures was evaluated between 200 and 600 °C, and the activation energy was
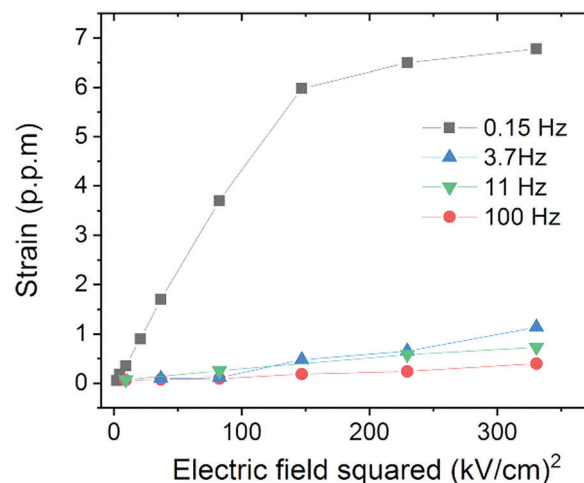

Fig. 2 Electromechanical strain of the CGO single crystal at room temperature for different electric field frequencies measured by laser interferometry (Fig. S1, ESI†). The electrostriction coefficients are reported in Table 1.

calculated to be 0.55 eV (Fig. S3, ESI†). This value is lower than that in polycrystalline samples (above 0.9 eV), probably due to the lack of an ionic blocking effect typical of grain boundaries.

Fig. 2 shows the sample electric field-induced strain (in ppm) for voltage frequencies from 0.15 Hz to 100 Hz. At 0.15 Hz, strain saturation and frequency relaxation are visible, as consistent with CGO ceramics.[4,14,37,38]

Table 1 reports the electrostriction coefficient for the corresponding frequency. These values are comparable to the polycrystalline CGO pellets previously reported.[4,14,37,38] Previous results indicate that the electrostriction effect is influenced by the blocking factor and vacancy clustering of the grain boundaries.[4,38] However, as the single crystal has a continuous lattice, the characterization here reported is not affected by structural variables and so it is ascribed solely to lattice distortions.

For the electromechanical effects at the lattice, we merged and normalized near L-III edge spectra (XANES) of Ce for room temperature (RT), −50 °C, −125 °C, and −194 °C. For each temperature, we report both ON and OFF states as well as the ON–OFF differences. We found that the electric field induces significant Ce local environment change, as evidenced by the differences between the 'ON' and 'OFF' states of the XANES spectra.

Fig. 3 summarises the results. Fig. 3a shows the main features of the Ce L-III edge spectra: the pre-peak, peak A and peak B, each of which represents a different electronic transition. Fig. 3b reports the difference between ON and OFF

Table 1 Electrostriction coefficient of CGO single crystal at the frequencies reported in Fig. 2

Electric field frequency (Hz)	0.15	3.7	11	100
$M_{33} \times 10^{-18}$ (m^2 V^{-2})	3.88	0.27	0.39	0.21

This journal is © the Owner Societies 2021

Phys. Chem. Chem. Phys., 2021, **23**, 11233–11239 | **11235**

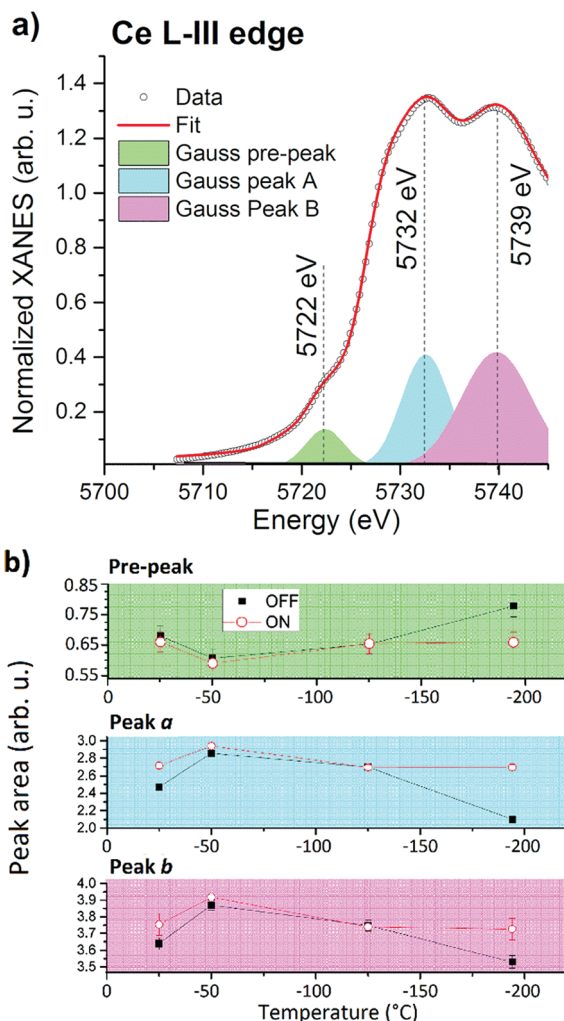{"type":"text"}

Fig. 3   (a) Schematics of the Ce L-III edge features position and Gaussian fitting: pre-peak feature at 5722 eV in green, Peak A at 5732 eV in light blue, Peak B at 5739 eV in purple. (b) Area of each feature for ON and OFF states at different temperatures. The numerical data are reported in Table S2 (ESI†).
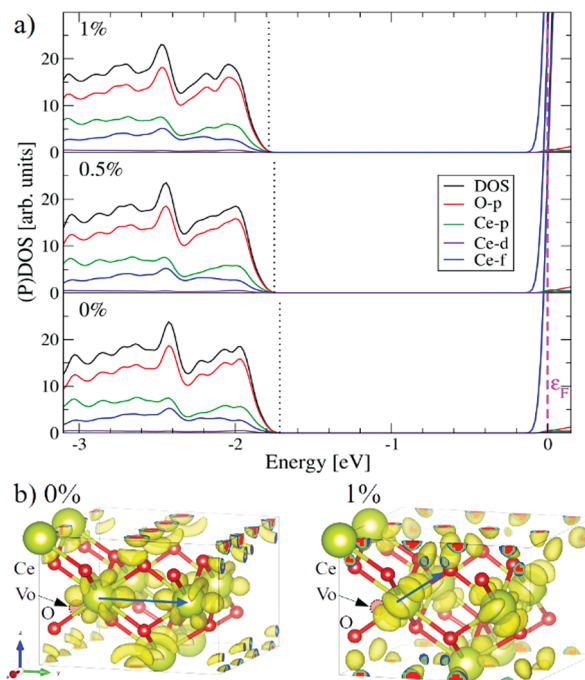

Fig. 4   (a) Density of states for different strains (projected); the valence band edge shifts to more negative energies with increasing strain due to a distortion of the structure. (b) The orbitals depicted correspond to the band at the valence band edge for the unstrained and 1% strained configuration. Ce atoms are indicated in yellow, O in red and the oxygen vacancy (V_O) in pink. The preferred direction of the orbitals is indicated with the blue arrow.

states of each feature for different temperatures. Table S2 in the ESI† reports the calculated values.

The pre-peak at 5722 eV was measured to decrease when an electric field is applied (Fig. 3b, green). By reducing the temperature, the difference in the areas became more prominent at −194 °C. The pre-peak feature corresponds to the $2p_{3/2} \rightarrow 4f$ transition, as an effect of 4f and 5d orbital hybridization.[39,40] Therefore at low temperature, 4f–5d hybridization appears to be blocked by the external electric field, while it seems negligible at room temperature.

Peaks A and B at 5730–5740 eV showed the opposite behaviour (Fig. 3b, light blue and purple): when we applied the electric field, the area of these features increased. Peaks A and B represent the transition $2p_{3/2} \rightarrow 5d$.[6,41] The increment in these features denotes stronger Ce–O bonds and, consequently, a more dominant ionic nature.[1,6,7,41] Such an effect proves that the electric field induces a distortion in a Ce cation's vicinity.[1,6,7] By decreasing the temperature, difference in the ON and OFF states becomes

higher, reaching roughly double the value between RT and −194 °C.

In summary, low temperatures affect the bond properties of Ce in the presence of an electric field. Cryogenic conditions promote crystal distortion and ionic behaviour while hindering the hybridization of 4f–5d orbitals. This effect, in particular, is visible only at low temperatures.

The DFT results in Fig. 4 confirm the finding. The density of states (DOS, Fig. 4a) shows that the distortion of the structure caused by the strain is responsible for shifting to more negative energies of the valence band edge. By more closely investigating the orbitals accountable for this effect, we also note that both O and Ce orbitals contribute to this shift. The DOS change can more easily be observed by plotting the orbitals at the valence band edge (Fig. 4b). Under strain, the orbitals, mostly pointing towards the Ce-ion, i.e. the [010] plane, as indicated by the blue arrow (left panel, 0%), now rotate and align with the Ce–O plane (right panel, 1%).

We performed Extended X-ray Absorption Fine Structure (EXAFS) measurements to clarify the structural mechanisms occurring in the electrostriction. As described in the ESI,† we fitted the first coordination shell around Ce (i.e. the nearest-neighbour oxygen atom). We report the results for $\chi(k)_{on}$ and $\chi(k)_{off}$ as well as the differential spectrum $\Delta\chi(k) = \chi(k)_{on} - \chi(k)_{off}$. In particular, Fig. 5a displays the EXAFS fit at RT under the 'ON' state. Fig. 5b shows the fitted RT differential $\Delta\chi(k)$ spectrum. The fit for the other temperatures is in the ESI† (Fig. S4). Table
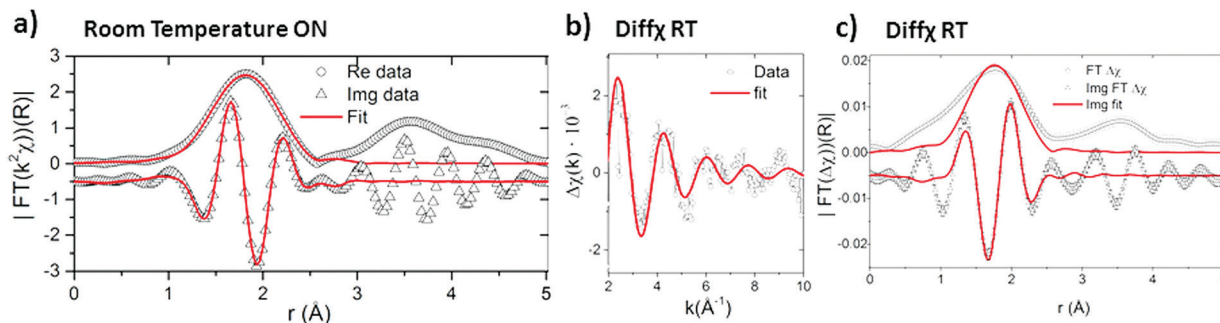
11236 | Phys. Chem. Chem. Phys., 2021, 23, 11233–11239

This journal is © the Owner Societies 2021

Fig. 5 (a) EXAFS fit of room temperature ON state spectrum. (b and c) Fits of the room temperature EXAFS differential spectrum $\Delta\chi(k) = \chi(k)_{on} - \chi(k)_{off}$. The fits for the other temperatures are in the ESI.†

Table 2 Difference in the bond length $\left(\frac{\Delta R - R_{Off}}{R_{Off}}\right)$ and the fraction ($\Delta N/N_{Off}$) of the electroactive pairs in the lattice at different temperatures. Maximum strain and stress are also reported, considering a constant CGO Young's modulus of 200 GPa[1,3]

T (°C)	R_{OFF}	N_{OFF}	ΔR	ΔN	$(\Delta R - R_{OFF})/R_{OFF}$ (%)	$\Delta N/N_{OFF}$ (%)	Strain $\times 10^{-4}$	Stress (MPa)
23	2.299	7.99	2.246	−0.19	−2.3(2)	2(1)	5.5(3.0)	110(60)
−50	2.300	7.99	2.250	−0.16	−2.17(3)	2(2)	4(5)	87(110)
−125	2.301	7.99	2.040	−0.33	−11.3(9)	4(10)	46(130)	937(2600)
−194	2.304	7.99	2.219	−0.99	−3.689(5)	12(2)	45(7)	914(140)

S3 (ESI†) contains the fit results for the ON and OFF states of $\chi(k)$ absorption spectra. The coordination number (same for all the dataset $N = 7.99 \pm 0.23$), the nearest neighbour bond length (R_{Ce-O}), and the bond disorder factor (σ^2) are reported. Table 2 also reports the values of N and R for the OFF state.

As reported in Table S3 (ESI†), we find that the Ce–O bond length is nearly constant with temperature; around 2.30 Å. These results are in general agreement with previous results.[6,39,42]

The differential analysis between the OFF/ON states allows for analysis of the strain induced by an electric field. The differential spectra $\Delta\chi$ are at different temperatures. Table 2 summarises the differential coordination number (ΔN), and bond length (ΔR) found from the fit. These results are reported in detail in Table S4 (ESI†). The fit coefficients are consistent with the results reported by Lubomirsky *et al.* for room temperature polycrystalline samples.[6] When cooled down, the ΔR_{Ce-O} value seems to change with an unclear pattern, suggesting that the magnitude of the electric field-induced distortion is not temperature-dependent.

The coordination number found was negative ($\Delta N = -0.2$ at room temperature), which indicates short Ce–O bonds that are electromechanically active.[6,7] Moreover, ΔN decreases from −0.2 at RT to −1 at −194 °C, indicating different bonding dynamics that increase the number of electroactive bonds. The calculated values also indicate that N decreases progressively with the temperature; however, the error bars for −50 and −125 °C are relatively high, and the effect needs further investigation.

We estimate both the fraction of the electroactive bonds and the maximum strain they can develop by comparing the coordination number and Ce–O bond length of the differential and OFF spectra. For instance, at room temperature, the electroactive pairs are about 2% of the total bonds ($\Delta N/N_{OFF}$). Additionally, the bond length of these pairs is ∼2.3% shorter (the

difference in bond length is ($\Delta R - R_{OFF}/R_{OFF}$)), suggesting that when an electric field is applied, the pairs can generate a maximum distortion on their domain that compensates the 2.3% strain.[6] Assuming that all of the pairs contribute equivalently to electrostriction, a strain of 0.055% can form. The assumption suits the single-crystal sample, where pairs have a similar configuration as we do not expect disorder-vacancies interactions.

Table 2 summarises the values calculated for a fraction of electroactive species and the theoretical maximum strain for different temperatures. At −194 °C, the population of electro-active pairs increases to 12%, six times as large as that at room temperature. Therefore, the maximum estimated strain is 4.5 × 10^{-3}. Considering that the elastic modulus of CGO is around 200 GPa,[1,3] the maximum mechanical stress is estimated to be 110 and 914 MPa at RT and −194 °C, respectively. Unfortunately, a definition of a general trend is problematic due to the significant noise at −50 and −125 °C.

Although direct measurement of the macroscopic strain is missing, our analysis of the crystal shows that the low temperatures favour electrostriction. A primary cause for the effect is the increase in the population of electroactive pairs in the lattice. Reduced vacancy mobility at lower temperatures can induce a stable pair and thus generate local charge anisotropy in the lattice. Another reason can be the cation/anion pair potential's asymmetry, which leads to cell distortion under approximately −150 °C.[23]

Conclusions

This work reports the electrostrictive properties of a 10 mol% Gd-doped ceria (CGO) single crystal at low temperatures.
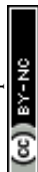
The sample displayed similar bulk properties to polycrystalline CGO, with frequency relaxation and strain saturation.

We performed *in situ* XAS techniques at the L-III edge of Ce, over a wide temperature range from RT to -194 °C. Analysis of the XANES spectra reveals an increase of the features representing the ionic behaviour of the cerium cations under an intense electric field of *ca.* 11 kV cm^{-1} (ON state). The effect increased at lower temperatures.

Differential EXAFS (ON–OFF spectrum) shows an average Ce coordination number (first shell) reduction and shortened Ce–O bond lengths when the electric field is applied. This result indicates an electroactive population that generates local mechanical strain, which changes the shape of the Ce orbitals. Instead of pointing in the [010] direction, the orbitals point along the direction of the Ce–O pair, which we show with DFT calculations. The PDOS analysis also shows that the valence band edge is pushed towards more negative energies for increasing applied strain. We demonstrate that low temperatures significantly increase the number of electrostrictive pairs (by six times from RT to -194 °C). We estimate the maximum expected strain to increase from 5.5×10^{-4} at RT to 4.5×10^{-3} at -194 °C. As the vacancy concentration is constant at low temperatures, this result suggests a heterogeneous population of the pairs with both electromechanically active and inactive configurations in the sample. Such a result in a single-crystal, *i.e.* with a low degree of crystalline disorder, suggests large-range, electrostatic and elastic interactions, *e.g.* in the nanometric domain.

Such interactions are temperature-dependent and can affect the pair configuration and, thus, the overall electromechanical properties.

Conflicts of interest

There are no conflicts of interest to declare.

Acknowledgements

References

1 R. Korobko, A. Patlolla, A. Kossoy, E. Wachtel, H. L. Tuller, A. I. Frenkel and I. Lubomirsky, *Adv. Mater.*, 2012, **24**, 5857–5861.

2 R. Korobko, E. Wachtel and I. Lubomirsky, *Sens. Actuators, A*, 2013, **201**, 73–78.

3 S. Santucci, H. Zhang, S. Sanna, N. Pryds and V. Esposito, *APL Mater.*, 2019, **7**, 071104.

4 A. Kabir, S. Santucci, N. Van Nong, M. Varenik, I. Lubomirsky, R. Nigon, P. Muralt and V. Esposito, *Acta Mater.*, 2019, **174**, 53–60.

5 M. Hadad, H. Ashraf, G. Mohanty, C. Sandu and P. Muralt, *Acta Mater.*, 2016, **118**, 1–7.

6 R. Korobko, A. Lerner, Y. Li, E. Wachtel, A. I. Frenkel and I. Lubomirsky, *Appl. Phys. Lett.*, 2015, **106**, 042904.

7 Y. Li, O. Kraynis, J. Kas, T. C. Weng, D. Sokaras, R. Zacharowicz, I. Lubomirsky and A. I. Frenkel, *AIP Adv.*, 2016, **6**, 055320.

8 A. Kossoy, A. I. Frenkel, Q. Wang, E. Wachtel and I. Lubomirsky, *Adv. Mater.*, 2010, **22**, 1659–1662.

9 A. Kossoy, A. I. Frenkel, Y. Feldman, E. Wachtel, A. Milner and I. Lubomirsky, *Solid State Ionics*, 2010, **181**, 1473–1477.

10 V. Esposito and E. Traversa, *J. Am. Ceram. Soc.*, 2008, **91**, 1037–1051.

11 S. Santucci, H. Zhang, S. Sanna, N. Pryds and V. Esposito, *J. Mater. Chem. A*, 2020, **8**, 14023–14030.

12 V. Sundar and R. E. Newnham, *Mater. Res. Bull.*, 1996, **31**, 545–554.

13 A. L. Kholkin, C. Wütchrich, D. V. Taylor and N. Setter, *Rev. Sci. Instrum.*, 1996, **67**, 1935–1941.

14 A. Kabir, H. Zhang, S. Colding-jørgensen, S. Santucci, S. Molin and V. Esposito, *Acta Mater.*, 2020, **187**, 183–187.

15 V. Esposito, D. W. Ni, S. Sanna, F. Gualandris and N. Pryds, *RSC Adv.*, 2017, **7**, 13784–13788.

16 H. Huang, M. Nakamura, P. Su, R. Fasching, Y. Saito and F. B. Prinz, *J. Electrochem. Soc.*, 2007, **154**, 20–24.

17 J. L. M. Rupp and L. J. Gauckler, *Solid State Ionics*, 2006, **177**, 2513–2518.

18 E. Mishuk, A. D. Ushakov, S. R. Cohen, V. Y. Shur, A. L. Kholkin and I. Lubomirsky, *Solid State Ionics*, 2018, **327**, 47–51.

19 A. D. Ushakov, E. Mishuk, E. Makagon, D. O. Alikin, A. A. Esin, I. S. Baturin, A. Tselev, V. Y. Shur, I. Lubomirsky and A. L. Kholkin, *Appl. Phys. Lett.*, 2017, **110**, 142902.

20 M. V. F. Schlupp, A. Kurlov, J. Hwang, Z. Yung, M. Döbeli, J. Martynczuk, M. Prestat, J. Son and L. J. Gauckler, *Fuel Cells*, 2013, **13**, 658–665.

21 G. Chiodelli, L. Malavasi, V. Massarotti, P. Mustarelli and E. Quartarone, *Solid State Ionics*, 2005, **176**, 1505–1512.

22 V. Shelukhin, I. Zon, E. Wachtel, Y. Feldman and I. Lubomirsky, *Solid State Ionics*, 2012, **211**, 12–19.

23 A. S. Nowick, *Solid State Ionics*, 2000, **136–137**, 1307–1314.

24 J. P. Eufinger, M. Daniels, K. Schmale, S. Berendts, G. Ulbrich, M. Lerch, H. D. Wiemhöfer and J. Janek, *Phys. Chem. Chem. Phys.*, 2014, **16**, 25583–25600.

25 K. Michel, J. P. Eufinger, G. Ulbrich, M. Lerch, J. Janek and M. T. Elm, *Phys. Chem. Chem. Phys.*, 2017, **19**, 17661–17669.

26 K. Neuhaus, F. Schulze-Küppers, S. Baumann, G. Ulbrich, M. Lerch and H. D. Wiemhöfer, *Solid State Ionics*, 2016, **288**, 325–330.

27 S. Berendts and M. Lerch, *J. Cryst. Growth*, 2011, **336**, 106–111.

28 L. Simonelli, C. Marini, W. Olszewski, M. Ávila Pérez, N. Ramanan, G. Guilera, V. Cuartero and K. Klementiev,

11238 | *Phys. Chem. Chem. Phys.*, 2021, **23**, 11233–11239

This journal is © the Owner Societies 2021

Cogent Phys., 2016, **3**(1), DOI: 10.1080/23311940. 2016.1231987.

29 B. Ravel and M. Newville, *Phys. Scr., T*, 2005, **T115**, 1007–1010.

30 P. J. E. M. Van Der Linden, M. Moretti Sala, C. Henriquet, M. Rossi, K. Ohgushi, F. Fauth, L. Simonelli, C. Marini, E. Fraga, C. Murray, J. Potter and M. Krisch, *Rev. Sci. Instrum.*, 2016, **87**, 0–11.

31 C. Marini, R. Boada, J. Prieto Burgos, N. Ramanan, I. García Domínguez, J. Zhao, T. T. Xiao and L. Simonelli, *Nucl. Instrum. Methods Phys. Res., Sect. A*, 2018, **908**, 333–337.

32 J. P. Perdew, K. Burke and M. Ernzerhof, *Phys. Rev. Lett.*, 1996, **77**, 3865–3868.

33 J. J. Mortensen, L. B. Hansen and K. W. Jacobsen, *Phys. Rev. B: Condens. Matter Mater. Phys.*, 2005, **71**, 35109.

34 J. Enkovaara, C. Rostgaard, J. J. Mortensen, J. Chen, M. Dułak, L. Ferrighi, J. Gavnholt, C. Glinsvad, V. Haikola, H. A. Hansen, H. H. Kristoffersen, M. Kuisma, A. H. Larsen, L. Lehtovaara, M. Ljungberg, O. Lopez-Acevedo, P. G. Moses, J. Ojanen, T. Olsen, V. Petzold, N. A. Romero, J. Stausholm-Møller, M. Strange, G. A. Tritsaris, M. Vanin, M. Walter, B. Hammer, H. Häkkinen, G. K. H. Madsen, R. M. Nieminen, J. K. Nørskov, M. Puska, T. T. Rantala, J. Schiøtz, K. S. Thygesen and K. W. Jacobsen, *J. Phys.: Condens. Matter*, 2010, **22**, 253202.

35 A. H. Larsen, J. J. Mortensen, J. Blomqvist, I. E. Castelli, R. Christensen, M. Dułak, J. Friis, M. N. Groves, B. Hammer, C. Hargus, E. D. Hermes, P. C. Jennings, P. B. Jensen, J. Kermode, J. R. Kitchin, E. L. Kolsbjerg, J. Kubal, K. Kaasbjerg, S. Lysgaard, J. B. Maronsson, T. Maxson, T. Olsen, L. Pastewka, A. Peterson, C. Rostgaard, J. Schiøtz, O. Schütt, M. Strange, K. S. Thygesen, T. Vegge, L. Vilhelmsen, M. Walter, Z. Zeng and K. W. Jacobsen, *J. Phys.: Condens. Matter*, 2017, **29**, 273002.

36 N. Goykhman, Y. Feldman, E. Wachtel, A. Yoffe and I. Lubomirsky, *J. Electroceram.*, 2014, **33**, 180–186.

37 A. Kabir, J. R. Bowen, M. Varenik, I. Lubomirsky and V. Esposito, *Materialia*, 2020, **12**, 3–8.

38 A. Kabir, J. Kyu Han, B. Merle and V. Esposito, *Mater. Lett.*, 2020, **266**, 127490.

39 A. M. Shahin, F. Grandjean, G. J. Long and T. P. Schuman, *Chem. Mater.*, 2005, **17**, 315–321.

40 J. C. Kuang, *Adv. Mater. Res.*, 2014, **1022**, 72–75.

41 F. Zhang, P. Wang, J. Koberstein, S. Khalid and S. W. Chan, *Surf. Sci.*, 2004, **563**, 74–82.

42 T. Ohashi, S. Yamazaki, T. Tokunaga, Y. Arita, T. Matsui, T. Harami and K. Kobayashi, *Solid State Ionics*, 1998, **113–115**, 559–564.

This journal is © the Owner Societies 2021

Phys. Chem. Chem. Phys., 2021, **23**, 11233–11239 | **11239**